Journal of Materials Chemistry A

ROYAL SOCIETY OF CHEMISTRY

PAPER

View Article Online
View Journal | View Issue

Cite this: J. Mater. Chem. A, 2025, 13, 795

Recyclable HF-free $Ti_3C_2T_x$ 3D-printed supercapacitors: their second life in sodium-ion batteries†

Bindu Kalleshappa[a] and Martin Pumera *[abc]

2D MXenes represent a useful class of materials in various applications and the main constraint for their bulk production is the requirement of hazardous hydrogen fluoride (HF) as an etching agent. Molten salt synthesis is one of the emerging HF-free techniques to produce MXenes, where a mixture of etching salts is heated till their melting point to etch the MAX phase. Here, we etched Ti_3AlC_2 MAX using the molten salt synthesis method to obtain 2D $Ti_3C_2T_x$, by lowering the typical high reaction temperature (~700 °C) to 400 °C using oxalic acid as an organic additive, which contributes in reducing the overall melting point of the etching salt mixture. Then, the electrochemical properties of $Ti_3C_2T_x$ were demonstrated by designing recyclable 3D printed supercapacitors using modified polylactic acid (PLA)/conductive graphene 3D electrodes. A real life application of recyclable 3D printed supercapacitors was demonstrated by powering a digital thermometer. Further, the used supercapacitors were recycled to collect the conductive carbon and constructed a sodium-ion battery using it as a conducting additive of the $Ti_3C_2T_x$ anode and powered up a glucometer. A zero-waste device with the 'concept 3R' (recycle, recover and reuse) reduces the carbon footprint by keeping the materials out of landfills. Concerning environmental safety and e-waste management, this work establishes a green synthesis of $Ti_3C_2T_x$ and demonstrates the use of recyclable materials in 3D printed devices for energy storage devices.

Received 18th October 2024
Accepted 19th November 2024

DOI: 10.1039/d4ta07436j

rsc.li/materials-a

Introduction

The energy crisis and e-waste are two global issues that go hand in hand. To satisfy the energy demand of the current world, new technologies of energy conversion and storage are being developed. In the process, the e-waste of energy storage devices is also growing with the energy storage industry. According to data, nearly 2 million metric tonnes of energy storage devices per year are ending up as environmentally undesirable, hazardous waste. An immediate action must be taken towards the concept of recycle, recover and reuse (3R) of energy storage devices to save the environment.[1–3] Spent energy storage devices are recyclable and can be considered as secondary sources of useful materials. Unfortunately, only 5% of them are recycled due to economic and technical reasons. One of the solutions for these issues is to use reusable and recyclable materials in the construction of an energy storage device.

Recently, 3D printed supercapacitors attracted researchers, because of the freedom to customize electrodes with different shapes and to choose additives with various properties. 3D printed energy storage devices are also reusable and recyclable. Since PLA is a biodegradable polymer that converts into lactic acid, conductive graphene/PLA 3D filament can be recycled to utilize it further for different applications to avoid the wastage of resources.[4,5] Despite their usefulness, 3D printed electrodes suffer from low surface conductivity, which affects the energy storage capability of supercapacitors.[6–10] In our previous work, we proposed the modification of 3D printed conductive graphene/polylactic acid (PLA) electrodes using MoS_2/MXene for energy storage.[11] Inspired by this work, several groups utilized MXenes to improve the surface conductivity of 3D printed electrodes, thereby improving the performance of supercapacitors.[12] In the current work, 3D printed supercapacitors will be designed using a green-technique synthesised MXene. MXenes are derived by etching MAX phases. MAX is a transition metal carbide or nitride or carbonitride layered material with a weakly bonded metal layer in-between. The structural formula of MAX can be written as $M_xA_yX_{x-1}$, where M

[a]Future Energy and Innovation Laboratory, Central European Institute of Technology, Brno University of Technology, Purkyňova 123, 61200 Brno, Czech Republic. E-mail: martin.pumera@ceitec.vutbr.cz

[b]Advanced Nanorobots & Multiscale Robotics Laboratory, Faculty of Electrical Engineering and Computer Science, VSB – Technical University of Ostrava, 17. Listopadu 2172/15, 70800 Ostrava, Czech Republic

[c]Department of Medical Research, China Medical University Hospital, China Medical University, No. 91 Hsueh-Shih Road, Taichung 40402, Taiwan

† Electronic supplementary information (ESI) available: Experimental materials and methods, SEM images, XPS, electrochemical studies and tables (PDF). Application of the TC-3DE supercapacitor to power a digital thermometer (Video S1). Application of $Ti_3C_2T_x$ with a recycled conductive graphene anode-based sodium-ion battery to power a glucometer (Video-S2). See DOI: https://doi.org/10.1039/d4ta07436j

is a transition metal (*e.g.*, Ti, V, Mo, Nb), A is a metal (Al, Si, and Sn) and X is C or N or CN. A general formula of MXenes can be written as $M_xX_{x-1}T_z$, where T_z represents the surface functional group resulting from the etching agent and the solution.[13–22]

MXenes are considered favourable materials in energy storage applications even though their exact charge storage mechanism is currently unknown. Among all MXenes, $Ti_3C_2T_x$ is the most studied active material because of its high electrical conductivity, high reactivity and better energy storage properties. Generally, the capacitive properties of $Ti_3C_2T_x$ are influenced by parameters, like interlayer spacing, types of terminal groups, the structure of the electrode and electrolytes. Designing MXene based supercapacitors with tailored properties is one of the interesting research areas to be explored.[23–27]

The most commonly used MAX etching agent is hydrogen fluoride (HF), which is a dangerous and highly toxic acid. Excessive exposure to this acid is hazardous to health and the environment.[28,29] To avoid the usage of HF, various research groups have introduced several etching agents and etching methods.[30–34] Molten salt synthesis (MSS) is one of the easiest and best methods to avoid HF exposure during the synthesis of MXenes. It is a clean and simple synthesis technique, which is simple and scalable. This can be optimized to scale up the MXene synthesis to the industrial level without the use of hazardous acids. In MSS, the reaction takes place in a closed system, so we are not exposed to the dangerous gasses or other substances that may form. In the molten salt synthesis, a mixture of salts is heated till it melts and this molten liquid is used as both a solvent and an etchant, to etch the 'A' layer of the MAX phase. The time and temperature of MSS can be optimized according to the final product requirements. Achieving a short diffusion length and high transport rate of molecules for a fast reaction is the main purpose of heating in MSS. The operating temperature of MSS should be higher than the melting temperature of reactant salts. To achieve this, a heterogeneous salt mixture will be used, which will have a low eutectic temperature. The ratio of the eutectic mixture and the operating temperature and time can be optimised to scale up MXene synthesis to the industrial level using MSS. Originally, Ti_4N_3 MXene was synthesized by etching Ti_4AlN_3 at 550 °C using a eutectic mixture of potassium fluoride (KF), lithium fluoride (LiF) and sodium fluoride (NaF) with a ratio of 0.59 : 0.29 : 0.12, respectively.[35]

Lately, different salt mixtures were used to etch titanium carbide effectively using the molten salt method (MSS) as per the requirements of the application.[36–38] Arole *et al.* synthesized a $Ti_3C_2T_z$ MXene nanosheet by melting tin fluoride (SnF_2) at 550 °C, which has a lower melting point and large atomic radius.[39] Similarly, Wang *et al.* modulated the cobalt content in $Ti_3C_2T_x$ MXene by etching the MAX phase using the MSS method in the presence of a $CoCl_2$: LiCl : KCl mixture for the purpose of the hydrogen evolution reaction. They found that cobalt (Co) atoms anchored on the MXene sheets improved their catalytic activity for the hydrogen evolution reaction.[40] The melting temperature of a mixture of salts can be lowered by selecting an appropriate eutectic ratio or by adding a suitable organic impurity with a low melting point.

We have introduced oxalic acid ($C_2H_2O_4$), which has a low melting point, as an operating temperature lowering additive in the MSS technique for MAX phase etching with a mixture of sodium fluoride (NaF) and potassium fluoride (KF). During the process, oxalic acid reacts with NaF and KF salts to form sodium and potassium salts of oxalic acid and hydrogen fluoride. The *in situ* HF formed during the reaction will etch the Ti_3AlC_2 MAX phase resulting in $Ti_3C_2T_x$ MXenes. The following are the proposed reactions during the MSS process in the presence of the oxalic acid additive with fluoride salts.[41]

$$H_2C_2O_4 + 2NaF \rightarrow Na_2C_2O_4 + 2HF$$

$$3HF + Ti_3AlC_2 \rightarrow AlF_3 + \tfrac{3}{2}H_2 + Ti_3C_2$$

$$Ti_3C_2 + 2HF \rightarrow Ti_3C_2F_2 + H_2$$

In the current work, the etching temperature of Ti_3AlC_2 was lowered to 400 °C by the addition of oxalic acid dihydrate as an additive, which has a melting point of 100 °C. Then, Ti_3C_2 modified 3D-printed supercapacitors were fabricated and recycled after use. The recycled conductive carbon and sodium lactate solutions were utilized as conductive additives in sodium-ion battery electrodes and an electrolyte, respectively. This article demonstrates the green synthesis of MXenes and environmentally friendly energy storage devices to address the issues of the energy crisis and e-waste management.

Materials and methods

Materials used

The titanium aluminium carbide (Ti_3AlC_2) MAX phase is purchased from Laizhou Kai Kai Ceramic Materials, China. pottasium fluoride (KF), sodium fluoride (NaF), oxalic acid dihydrate ($C_2H_2O_4$ $2H_2O$), xanthan gum, tetrabutyl ammonium hydroxide (TBAOH), ammonium per sulphate (APS), ethanol, sulphuric acid (H_2SO_4), polyvinylidene fluoride (PVDF), 1-methyl pyrrolidone (NMP), sodium perchlorate ($NaClO_4$), fluoroethylene carbonate (FEC), ethylene carbonate (EC) and diethylene carbonate (DEC) were purchased from Sigma Aldrich. Polylactic acid (PLA)/conductive graphene filament (BLACKMAGIC3D) is used for the 3D printing. All chemicals were used with no further purification.

Preparation of $Ti_3C_2T_x$ using the molten-salt synthesis method (MSTC-OX and MSTC-00)

A stoichiometric ratio of Ti_3AlC_2, NaF , KF (1 : 3, Al : F) and 1 g of oxalic acid dihydrate are mixed and ground in a mortar finely to get a uniform mixture. Then the mixture is transferred into an alumina tray with a lid and heated in a tube furnace at 400 °C for 8 hours in a nitrogen atmosphere. Then, the resultant powder was washed with de-ionized water (DIW), ethanol and ammonium persulphate solution (APS) to remove excess salt and the impurities. The resultant powder was dried at 60 °C in a vacuum oven overnight. The resultant sample is named MSTC-OX.

The above procedure is repeated without oxalic acid dihydrate, only with a mixture of Ti_3AlC_2, NaF and KF (1 : 3, Al : F ratio). The resultant sample is named MSTC-00.

Preparation of ExTC-OX ink

100 mg of MSTC-OX is added to 10 ml of TBAOH and sonicated in a bath ultra-sonicator at room temperature for 8 hours. Then, the TBAOH is removed by washing with ethanol and centrifuging. Then, the resultant sediment was dispersed in 10 ml of DIW and sonicated for 2 hours to obtain the ExTC-OX ink.

Fabrication and activation of 3D-printed nanocarbon electrodes (3DEs)

Lollipop shaped 3D electrodes with a 12 mm diameter were designed using Autodesk Fusion Lab 360 software and the design was sliced and exported to G-code which is the compatible file for printing on Prusa 3D printers. A commercial BLACKMAGIC3D (PLA/Conductive Graphene) filament is used to print the electrodes. The filament temperature and bed temperature are set to 220 °C and 60 °C, respectively.

Activation of 3D-printed black magic electrodes (3DEs)

The 3D-printed PLA/conductive graphene electrodes were chemically activated by keeping them in 1 M NaOH for 3 hours. After 3 hours, the electrodes were collected from the solution, washed with de-ionized water and dried in a vacuum oven at 40 °C for 6 hours.

Modification of activated 3DEs

The activated electrodes were modified by drop casting the ExTC-OX ink on the activated black magic electrodes and followed by drying at room temperature in a vacuum oven overnight. The modified 3DEs are named TC-3DE. TC-3DEs have ~0.5 mg of active material.

Preparation of 1 M H_2SO_4-xanthan gel electrolyte

1M H_2SO_4-xanthan gel electrolyte is prepared by mixing and stirring 100 mg of xanthan in 10 ml of 1 M H_2SO_4 solution at room temperature until we get a homogeneous viscous gel. The homogeneous gel is used as the electrolyte in symmetric supercapacitors.

Assembling symmetric TC-3DE supercapacitors

Symmetric TC-3DE supercapacitors were assembled by sandwiching ~200–300 μl of 1 M H_2SO_4-xanthan gel on a glass fiber separator between two TC-3DE electrodes.

Recycling of conductive carbon from the spent supercapacitors and waste black magic filament

The used 3D printed supercapacitors were recycled to obtain conductive carbon black in the 3D printed electrodes. The cells were disassembled to collect the electrodes. The collected electrodes were sonicated in de-ionised water for an hour and in ethanol for 30 min. Then, the cleaned electrodes were added into an aqueous solution of 1 M NaOH and left for 12 hours. Then the solution was sonicated for 30 min to dissolve the 3D printed electrodes. The obtained black colored solution was centrifuged to obtain the carbon black (CB). The supernatant solution is the sodium salt of lactic acid and the precipitate is the conductive carbon black. The supernatant was later filtered to utilize as electrolyte and the precipitate was washed multiple times with DIW and ethanol to utilize as a conductive additive in the electrodes. The washed CB was dried in a vacuum oven at 60 °C overnight and named RCB.

Carbon black from the fresh 3D filament is extracted using a similar procedure and the obtained carbon black is named 3DE-CB.

Assembling a sodium-ion cell using recycled conductive carbon black (RCB)

The electrodes were prepared by coating a mixture of MSTC-OX, RCB/super-p carbon black (SPCB) and PEO (7 : 2:1) in ethanol on Cu foil, followed by drying at 80 °C overnight in a vacuum oven. Each electrode has ~1.5 mg (1 mg cm^{-2}) of the active material. Sodium-ion half cells were assembled in a glove box with an Ar atmosphere by using Na foil as the anode, the MSTC-OX electrode and 250 μl of 1 M $NaClO_4$ in EC/DEC (1 : 1) FEC (5%) as the electrolyte in Swagelok cells.

SIB-a: MSTC-OX cathode with RCB|$NaClO_4$ electrolyte|Na-metal.

SIB-b: MSTC-OX cathode with SPCB|$NaClO_4$ electrolyte|Na-metal.

SIB-c: MSTC-OX cathode with 3DE-CB|$NaClO_4$ electrolyte|Na-metal.

Material characterization

The synthesised materials were characterized using powder X-ray diffraction (PXRD) to understand the crystal structure (Rigaku SmartLab 3 kW) with CuKα X-rays and the patterns were analysed using X'Pert HighScore Plus software. Raman spectroscopy is carried out using a WITEC Raman spectrometer with a 532 nm excitation source. Scanning electron microscopy (SEM) and energy dispersive X-ray spectroscopy (EDAX) (SEM, FEI VERIOS 460L, EDS EDAX SDD Octane Super) were performed to study the morphology and the elemental composition. X-ray photoelectron spectroscopy with an Al Kα monochromatic excitation source (XPS, Kratos AXIS Supra) is carried out and CASA XPS software was used to analyse the elemental composition of the materials. The background of the spectra was corrected using a linear function and Ti 2p and Al 2p, and elemental spectra were fitted using asymmetric Gaussian–Lorentzian curves. The non-carbide contaminants at the surface, like carbon and oxygen-based impurities (C–C, CH_x, C–OH, COO or OH), in C 1s, O 1s, and F 1s spectra were fitted using symmetric Gaussian–Lorentzian curves.

Electrochemical studies. To study the electrochemical properties of the TC-3DE electrodes and TC-3DE supercapacitors, cyclic voltammetry (CV), galvanostatic charge–discharge (GCD) and Electrochemical Impedance Spectroscopy (EIS) were carried out using a Metrohm Autolab potentiostat

(PGSTAT 204, The Netherlands) electrochemical workstation (NOVA 2.1 software). A three-electrode system is used to study the TC-3DE electrode where TC-3DE is used as the working electrode, a Pt wire is used as the counter electrode and Ag/AgCl (3 M KCl) is used as the reference electrode in 1 M H_2SO_4 electrolyte.

The electrochemical properties of the TC-3DE symmetric supercapacitors were studied by carrying out CV, GCD and EIS using a two-electrode system with 1 M H_2SO_4-xanthan gel electrolyte. The Nyquist plots of devices were fit using EC-Lab software.

The specific capacitance of the electrode is evaluated using the equation

$$C_s = \frac{i \times \Delta t}{m \times \Delta V}$$

where C_s is the specific capacitance in F g^{-1}, i/m is the current density in mA g^{-1}, Δt is the discharge time in s and ΔV is the potential window to discharge the cell in V.

The energy density and the power density of the cell are estimated using the equations,

$$E = \frac{1}{2} C_s \Delta V^2 \times \frac{1000}{3600}$$

$$P = \frac{E}{\Delta t}$$

where E (W h kg^{-1}) is the energy density, C_s (F g^{-1}) is the specific capacitance, ΔV (V) is the potential window and Δt (s) is the discharge time of the cell in GCD.

Similarly, the properties and the performance of the $Ti_3C_2T_x$ sodium-ion cell are studied by carrying out CV, EIS and GCD. The specific capacity of the anode is calculated using the formula

$$Q_s = \frac{I}{m} \times \Delta t$$

where Q_s (mA h g^{-1}) is the specific capacity, I (mA) is the applied current, m (g) is the mass of the active material and Δt (hour) is the charge/discharge time.

The current applied to the SIB cells in terms of C-rate is calculated using the formula

$$I = (\text{mass of the active material, g}) \times (\text{theoretical capacity, mA h } g^{-1}) \times (\text{C-rate})$$

Results and discussion

A schematic representation of the synthesis and exfoliation of $Ti_3C_2T_x$ MXene is shown in Fig. 1. In a typical synthesis, the Ti_3AlC_2 MAX phase was mixed with KF : NaF : oxalic acid dihydrate in a stoichiometric ratio. Then the mixture was heated at 400 °C under a N_2 atmosphere for 8 hours. The black powder obtained was washed and characterized. To confirm the complete etching of Al layers and the formation of the $Ti_3C_2T_x$ MXene phase, X-ray diffraction (XRD) was performed for the sample prepared without oxalic acid dihydrate (MSTC-00) and with oxalic acid dihydrate additive (MSTC-OX) samples and compared with the XRD pattern of the Ti_3AlC_2 MAX phase. Fig. 2A shows the XRD patterns of the Ti_3AlC_2 MAX phase, MSTC-00 and MSTC-OX samples. The XRD pattern of the Ti_3AlC_2 MAX phase matches that of ICDD 00-052-0875. It has a hexagonal crystal structure which belongs to the P63/mmcE space group (194). From the XRD pattern of MSTC-00, we can observe that the Al layer is not etched from the MAX phase. Meanwhile, on adding oxalic acid during molten salt synthesis of MSTC-OX, the Al layer is etched well, which is indicated by the shift and broadness of peaks. After etching the Al from the MAX phase in the case of MSTC-OX, the peaks shifted to lower 2θ in the $Ti_3C_2T_x$ MXene phase, which indicates an increased interlayer spacing. The characteristic peaks observed at 6.9°, 9.5°, 19.07° and 38.76° belong to (0 0 2), (0 0 2), (0 0 4), and (1 0 4) planes, respectively, representing the MXene formation. An increase in the broadness of the peaks indicates a loss of crystallinity after the removal of the aluminium layer from the MAX phase. The most intense peak in the MAX phase is at 38.76°, which represents the (1 0 4) plane and contains two Ti and two Al atoms.[42] Upon etching of the Al layer, the intensity of the peak is reduced and also the peaks in between 34° and 39° disappear in the case of MSTC-OX.

The (0 0 2) peak of the MAX phase at 9.64 shifted to 9.5° and 6.9° in the case of MSTC-OX, which indicates two different *d*-spacings in the samples. The spacing between the parallel neighbouring nanosheets is the *d*-spacing between the atomic planes of a crystal in MXenes, which is also called the c-lattice parameter (c-LP).[43] The c-LP of Ti_3AlC_2 (18.56 Å) is shifted to 25.72 Å upon removing the Al layers. Different *d*-spacings of titanium carbide MXene from various methods are tabulated in Table S1.†

The Raman spectra of Ti_3AlC_2 and MSTC-OX are shown in Fig. 2B. The characteristic vibrations of Ti_3AlC_2 are 267, 410 and 605 cm^{-1}, which belong to the shear and longitudinal oscillations of Ti and Al, which are observed in both samples.[44] The broadness of peaks in MSTC-OX increased due to the decreased crystallinity of the etched Al layer. Also, in the case of MSTC-OX, we can observe two broad peaks in the range of 1000–1800 cm^{-1}, which are due to the presence of carbon disorders.[44] The peaks at 1358 and 1597 cm^{-1} can be attributed to the D and G bands of carbon, respectively.[45] The intensity of D and G carbon bands increases upon etching, due to greater exposure of carbon on the surface of the $Ti_3C_2T_x$ MXene. We can observe a weak and broad peak at around 2900 cm^{-1} in MSTC-OX, which can be attributed to symmetric and asymmetric CH_2 vibrations.[46] Both XRD and Raman analyses confirm the proper etching of the Al layer from Ti_3AlC_2 in the presence of oxalic acid.

Scanning electron microscopy (SEM) helps us to visualize the etching of the Al layer from Ti_3AlC_2 with a separated layered morphology. To study the morphology and the elemental distribution of Ti_3AlC_2 and $Ti_3C_2T_x$ (MSTC-OX), SEM and energy dispersive X-ray spectroscopy (EDS) analyses of the samples were performed. Fig. 3A and B show the SEM images of Ti_3AlC_2 at different magnifications. We can observe a bulk layered

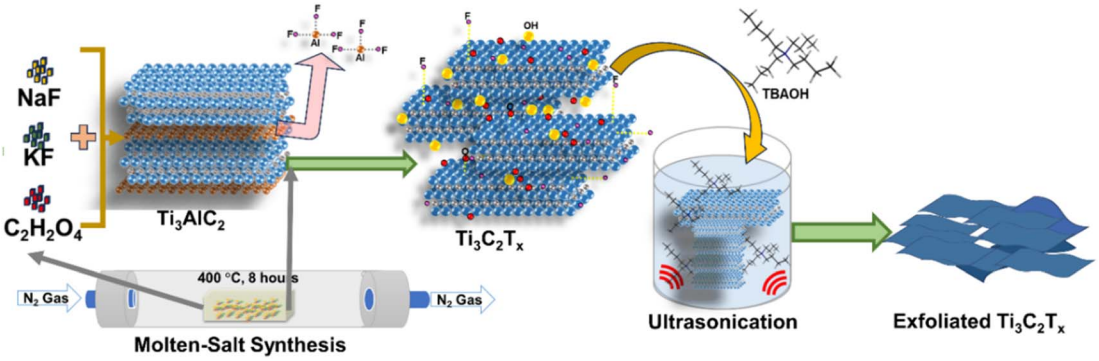

Fig. 1 Molten salt synthesis: a schematic representation of the molten-salt synthesis and exfoliation of $Ti_3C_2T_x$ MXene.

morphology, where Ti, C and Al are bonded strongly in the structure. The layers are separated in the SEM images of MSTC-OX (Fig. 3D and E), indicating etching of the Al layer from the MAX phase. Fig. 3D shows the morphology of $Ti_3C_2T_x$, which has an accordion structure after etching in the presence of oxalic acid. Meanwhile, there is no change in the morphology of the sample that has undergone molten salt treatment in the absence of oxalic acid (shown in Fig. S1†). A few nanometres thick separated layers of $Ti_3C_2T_x$ MXene can be observed in Fig. 2E. The EDS spectra of Ti_3AlC_2 and MSTC-OX are shown in Fig. 3C and F, respectively. We can observe the presence of fluorine, sodium and potassium in MSTC-OX, which indicates the etching of the aluminium layer by fluorine. The sodium and potassium impurities are from the KF and NaF precursors. The distribution of elements Ti Kα, F Kα, C Kα, O Kα, and Al Kα in the MSTC-OX samples can be observed in Fig. 3G. The matching bright spots in Al and O EDS maps indicate the presence of Al traces in the form of Al_2O_3.

XPS was used to analyse the elemental composition of the samples. Fig. 4A shows the XPS wide spectra of Ti_3AlC_2, MSTC-00, and MSTC-OX. In Fig. 2A, we can observe the presence of Ti 2p, Al 2p, C 1s and O 1s peaks in all the samples. Meanwhile, MSTC-OX has an extra F 1s peak, which represents the fluorine terminal groups.

Fig. 4B shows the Ti 2p high-resolution spectrum of MSTC-OX. Ti 2p components consist of $2p_{3/2}$ and $2p_{1/2}$ doublets due to atomic spin–orbit interaction. The intensity ratio restriction between $2p_{3/2}$ and $2p_{1/2}$ peaks was set as 2 : 1 while fitting. The Ti 2p XPS spectra of all of the samples were deconvoluted into 3 pairs of Ti $2p_{3/2}$ and Ti $2p_{1/2}$ of different bonds. In the case of Ti_3AlC_2 (Fig. S2(A)†), peaks at 454.4 eV, 455.7 eV, and 458.7 eV belong to Ti $2p_{3/2}$ of Ti–C, Ti–C–T_o and Ti–O, respectively. There is a small shift in all of the peaks in the case of MSTC-00 (Fig. S3(A)†) after molten salt treatment, but there is no peak corresponding to the Ti–F bond. The Ti $2p_{3/2}$ peaks that appear in MSTC-00 are 455.2, 456.6 and 459.3 eV, which represent Ti–C, Ti–C–T_o and Ti–O, respectively. Meanwhile, in the case of MSTC-OX, we observe Ti $2p_{3/2}$ peaks belonging to Ti–C, Ti–C–T_F and Ti–O at 455.3, 456.6 and 459.6 eV, respectively.[47]

The high-resolution elemental spectra of Al 2p of MSTC-OX are shown in Fig. 4C. The intensity of the Al 2p peak in MSTC-OX has reduced, which indicates the removal of the Al layer from Ti_3AlC_2. Only in the MSTC-OX sample, Al 2p has only one component belonging to Al_2O_3 at 75.1 eV (Al $2p_{3/2}$) and

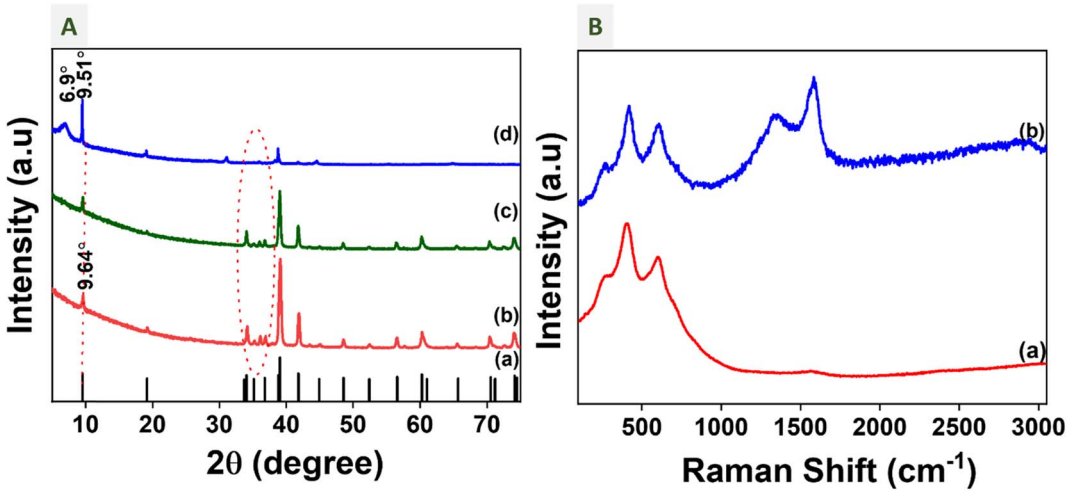

Fig. 2 Structural characterization: (A) XRD patterns of (a) ICDD 00-052-0875, (b) Ti_3AlC_2, (c) MSTC-00, and (d) MSTC-OX, and (B) Raman spectra of (a) Ti_3AlC_2 and (b) MSTC-OX.

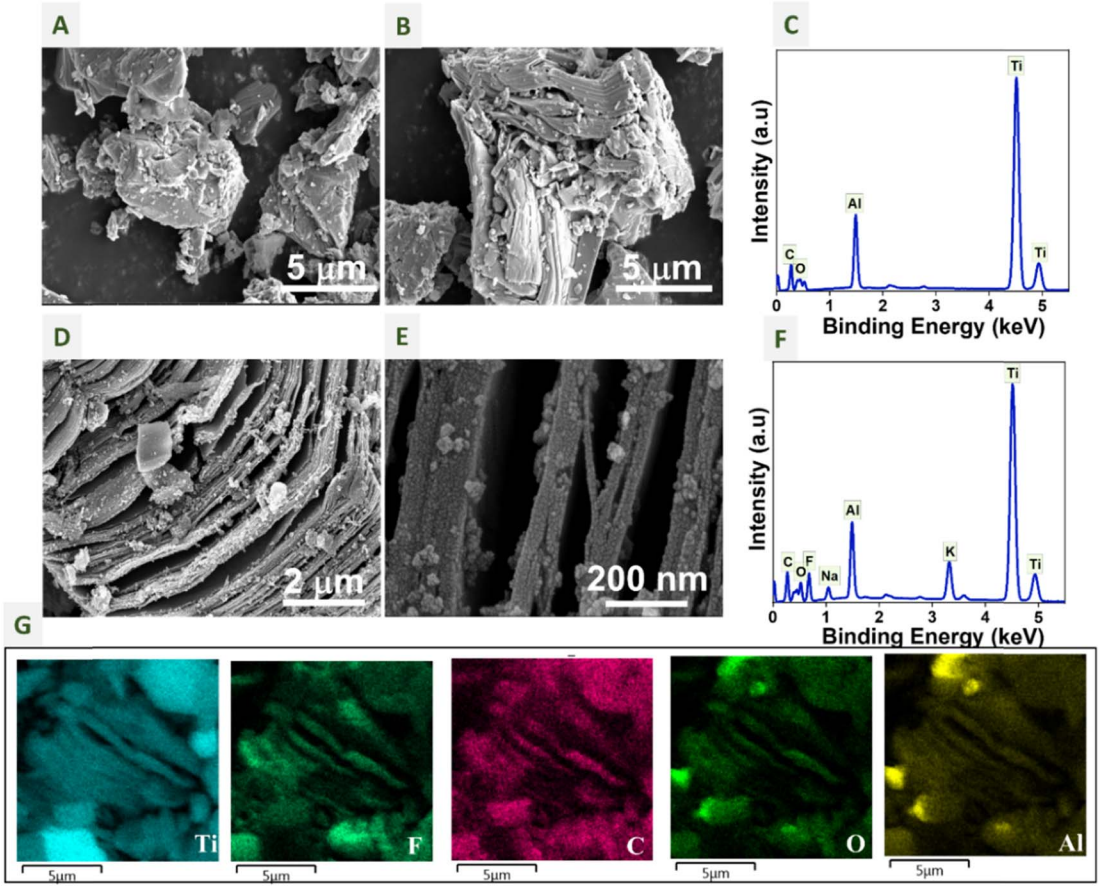

Fig. 3 Morphological and compositional characterization: SEM images of (A and B) Ti_3AlC_2, (D and E) MSTC-OX, energy dispersive X-ray spectra of (C) Ti_3AlC_2 and (F) MSTC-OX and EDS mapping of MSTC-OX for the elements (G) Ti Kα, F Kα, C Kα, O Kα, and Al Kα (left to right).

75.5 eV (Al $2p_{1/2}$), whereas in Ti_3AlC_2 and MSTC-00 samples (Fig. S2(B) and S3(B),† respectively), there are peaks belonging to metallic Al at 71.7 and 71.4 eV, respectively.[48–50]

The F 1s peak appears only in MSTC-OX, which indicates the inclusion of fluorine groups at the surface of $Ti_3C_2T_x$ terminal groups upon molten salt treatment. The F 1s peak is resolved into 685.2 and 686.8 eV peaks, which are shown in Fig. 3F, belonging to C–Ti–F and AlF_x components, respectively.[51] The removal of the Al layer from Ti_3AlC_2 by etching and the inclusion of fluorine at the terminal groups of MSTC-OX is also confirmed by the EDS analysis. The high-resolution spectra of elements of Ti_3AlC_2 and MSTC-00 are provided in ESI Fig. S2 and S3.† From XRD, EDS and XPS analyses, we can observe that oxalic acid helps to reduce the reaction temperature of the molten salt synthesis without causing any structural or compositional changes in the product.

Electrochemical properties of TC-3DE 3D-printed electrodes

The electrochemical properties of MSTC-OX compared to commercial Ti_3C_2 (etched using conventional HF-etching) are studied using a three-electrode system with 0.25 M Na_2SO_4 as an electrolyte. MSTC-OX and Ti_3C_2 coated carbon cloths were used as working electrodes. Ag/AgCl (3 M KCl) and a Pt wire were used as reference and counter electrodes, respectively. The Nyquist plots and cyclic voltammograms at 10 mV s^{-1} of MSTC-OX and Ti_3C_2 are shown in Fig. S4(A) and (B),† respectively. Both electrodes show similar impedance behaviour. The electrochemical area under the CV curves for MSTC-OX and Ti_3C_2 at 10 mV s^{-1} is ~0.377 and 0.379 A V^{-1} g^{-1}, respectively.

The synthesised MSTC-OX was exfoliated using TBAOH. The SEM image of exfoliated ExTC-OX is shown in Fig. 5A. The electrochemical properties of delaminated $Ti_3C_2T_x$ were studied by drop casting the ExTC-OX ink on NaOH activated PLA/conductive graphene electrodes. The XRD patterns of activated PLA/conductive graphene 3DE and ExTC-OX ink modified 3DE (TC-3DE) are shown in Fig. 5B. The SEM images of activated 3DE and ExTC-OX ink modified 3DE are shown in Fig. S5(A) and S5(B),† respectively. The XRD pattern of the activated PLA/conductive graphene 3D-printed electrode matches the reported pattern.[47] It has a PLA broad peak at around 10–30° with shoulder peaks at around 25.47° and 26.65°, which indicate the presence of a honeycomb graphene structure in the commercial Blackmagic3D printing filament.[52,53] TC-3DE has peaks belonging to $Ti_3C_2T_x$ MXene and PLA/conductive graphene.

The electrochemical performance of TC-3DE is studied using a three-electrode system. TC-3DE, a Pt wire and Ag/AgCl (3 M KCl) were used as working, counter and reference electrodes,

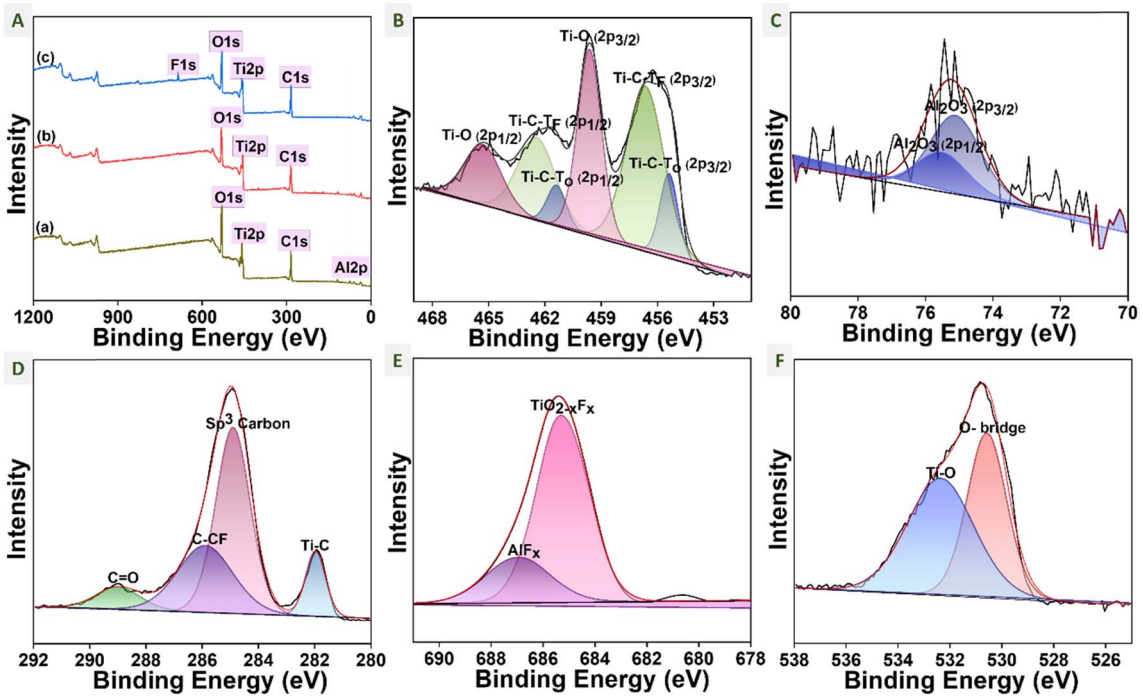

Fig. 4 Elemental composition of MSTC-OX: (A) XPS wide energy spectra of Ti_3AlC_2, MSTC-00 and MSTC-OX (down to up). High resolution elemental (B) Ti 2p, (C) Al 2p, (D) C 1s, (E) F 1s, and (F) O 1s spectra of MSTC-OX.

respectively, in 1 M H_2SO_4. Fig. 5C shows the cyclic voltammogram of TC-3DE and bare activated 3DE at a scan rate of 10 mV s^{-1}. The area under the CV of TC-3DE is 80 times greater than that of bare 3DE, which indicates that the high capacitance of TC-3DE is mainly due to the contribution from exfoliated $Ti_3C_2T_x$ sheets, and bare 3DE has an insignificant contribution to charge storage. The quasi-rectangular shapes with no redox peaks indicate the electrochemical double-layer capacitance

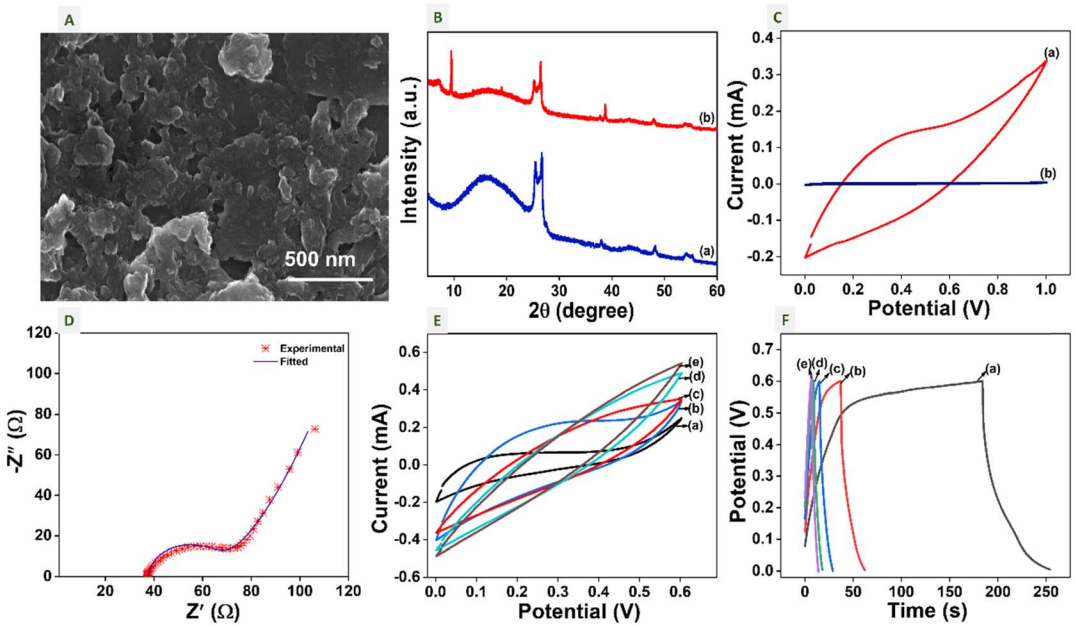

Fig. 5 Electrochemical studies of the TC-3DE electrode: (A) SEM image of EXTC-OX, (B) XRD patterns of (a) activated 3DE and (b) TC-3DE, (C) cyclic voltammograms of (a) bare activated 3DE and (b) TC-3DE, (D) Nyquist plot, (E) cyclic voltammograms at different scan rates ((a) 2, (b) 10, (c) 30, (d) 70, and (e) 100 mV s^{-1}) and (F) GCD curves at different current densities ((a) 200, (b) 300, (c) 400, (d) 500, and (e) 600 mV s^{-1}) of TC-3DE in 1 M H_2SO_4 against Ag/AgCl (3 M KCl).

(EDLC) behaviour of the electrodes. The absence of redox peaks in the CV indicates the absence of pseudo-capacitive behaviour. The trivial distortion of the EDLC behaviour can be related to the terminal functions on the $Ti_3C_2T_x$ nanosheets.[54] The current response of the electrodes is mostly capacitive for the voltage window of 0 to 1 V (*vs.* Ag/AgCl), which is in good agreement with previous studies on TiC MXenes.[54,55]

The electrical impedance and diffusion characteristics of TC-3DE were investigated using EIS. It is a critical technique to study electron/ion transportation in an electrochemical system. The physical processes, like mass diffusion, adsorption, chemical reaction and interfacial phenomenon, can be evaluated using the EIS technique. In the case of supercapacitors, the De Levie model depicts the electrode behaviour through the EIS nature. This model explains the ion diffusion and EDLC formation on the surface and within the porous electrode.[56] The Nyquist plot of TC-3DE is shown in Fig. 5D. We can observe a single semicircle in the high frequency region with a tail in the low frequency region. The low radius of the semicircle indicates a low charge transfer resistance (R_{ct}) along with a vertical line in the low frequency region, which represents the capacitive behaviour of the system.[57] The Randomize and Simplex method was used in EC-Lab software to fit the Nyquist plot to the equivalent circuit. The equivalent circuit fit for the curve is R_s + CPE/(R_{ct} + W_d), where R_s represents the solution resistance of the system and its value is 38 Ω. C_{dl} represents the capacitance of the electrode and CPE (constant phase element) represents the small pseudocapacitive behaviour of the electrode. The Bode plot of TC-3DE in Fig. S5(C†) reveals a phase angle value of −35° at lower frequency, which indicates the capacitive tendency of the electrode.[58]

The electrochemically active surface area (EASA) contributing to the excellent charge storage is estimated by carrying out cyclic voltammetry at different scan rates, as shown in Fig. 5E. The EASA is defined as[59]

$$\mathrm{EASA} = \frac{C_{dl}}{C_s},$$

where C_{dl} is the double layer capacitance estimated using the slope of the graph $\frac{\Delta j}{2}$ *versus* scan rate (ν). $j = |j_a - j_b|$ at a voltage where the electrode mostly shows capacitive behaviour. In our case, we selected the middle voltage, 0.3V, for the estimation of the EASA. Fig. S5(D†) shows the plot of $\frac{\Delta j}{2}$ *versus* ν, where we can see two slopes at different scan rates. In the range of 2 to 30 mV s^{-1}, the EASA is estimated to be ∼38 m^2 g^{-1} and in the range of 40 to 100 mV s^{-1}, it is ∼12 m^2 g^{-1}. The reason for the reduction in the electrochemically active surface area at a higher scan rate is due to the lack of time required for the interaction of the active species with the electrolyte.[60,61] Fig. 5F shows the galvanostatic charge–discharge (GCD) of TC-3DE at different current densities in the potential window of 0 to 0.6 V. The electrode has a specific capacitance of 68 F g^{-1} at a current density of 300 mA g^{-1}. The energy density and the power density of the electrode are 54.174 W kg^{-1} and 1.55 W h kg^{-1}, respectively. The comparative performance of the TC-3DE cell with reported 3D-printed supercapacitors is tabulated in Table S2.†

Electrochemical properties of symmetric TC-3DE supercapacitors

The electrochemical properties of symmetric TC-3DE supercapacitors with 1 M H_2SO_4 xanthan gel electrolyte are studied using different electrochemical techniques. The impedance properties of the symmetric TC-3DE supercapacitor were studied using EIS. The Nyquist plot and Bode impedance plot of the symmetric cell are given in Fig. 6A and B. The *x*-axis intercept in the high frequency region represents the electrical resistance of the device, which is known as the equivalent series resistance (ESR), also denoted as R_s.[62] The semicircle in the high frequency to mid-frequency region is due to the double layer formation. In this case, there is an initiation of the first semicircle at higher frequency, from which the charge transfer resistance (R_{ct1}) of the device is estimated to be 65 Ω. The R_{ct2} from the second semicircle is ∼40 Ω. Since it is a deformed semicircle, the capacitor can be replaced by a constant phase element (CPE). The vertical line in the low-frequency region is due to the ion diffusion between the electrode and electrolyte. Due to the presence of Warburg impedance, the ideal vertical line is a little deviated representing the near ideal capacitive behaviour of the devices.[63,64] The Bode plot in Fig. 6B shows the variation of impedance and the phase angle with respect to the frequency. The device shows a capacitive behaviour in the low frequency region and a resistive behaviour in the high frequency region. We can observe a single broad relaxation at a frequency of 1.7 Hz and the relaxation time (τ_0) is estimated to be 93 ms, which is a measure of time to discharge the device.[65]

The cyclic voltammograms of the symmetric TC-3DE supercapacitor at different scan rates are given in Fig. 6C. Further, the power law is used to deconvolute the charge storage mechanism into the capacitive and diffusion-controlled contributions of TiC-3DE. The power law[11] is given by

$$i = a\nu^b$$

$$\log(i) = b\log(\nu) + \log(a)$$

where 'i' is the current in A, 'ν' is the scan rate in mV s^{-1}, and a and b are proportionality constants. The value of constant 'b' indicates the charge storage mechanism of the system. $B = 0.5$ indicates the diffusion-controlled behaviour, $b = 1$ indicates the capacitive behaviour and $0.5 < b < 1$ indicates the contribution from both of the mechanisms in the electrodes. Fig. S6(A†) shows the plot of log(i) *vs.* log(ν). The slope of the plot is b = 0.78, which indicates the combinations of both capacitive and diffusion-controlled behaviours.

Further, the charge storage capacity of the symmetric TC-3DE cell in the potential window of 0 to 0.6 V is studied using the galvanostatic charge–discharge technique at different current densities. Fig. 6D shows the GCD curves of the symmetric TC-3DE cell at 150, 200 and 250 mA g^{-1} current densities. The specific capacitance of the cell at 150 mA g^{-1} current density is 30.8 F g^{-1}. The energy density and the power density of the cell are 1.767 W h kg^{-1} and 20.64 W kg^{-1}, respectively. A series combination of three symmetric TC-3DE cells was enough to power a digital thermometer, as shown in

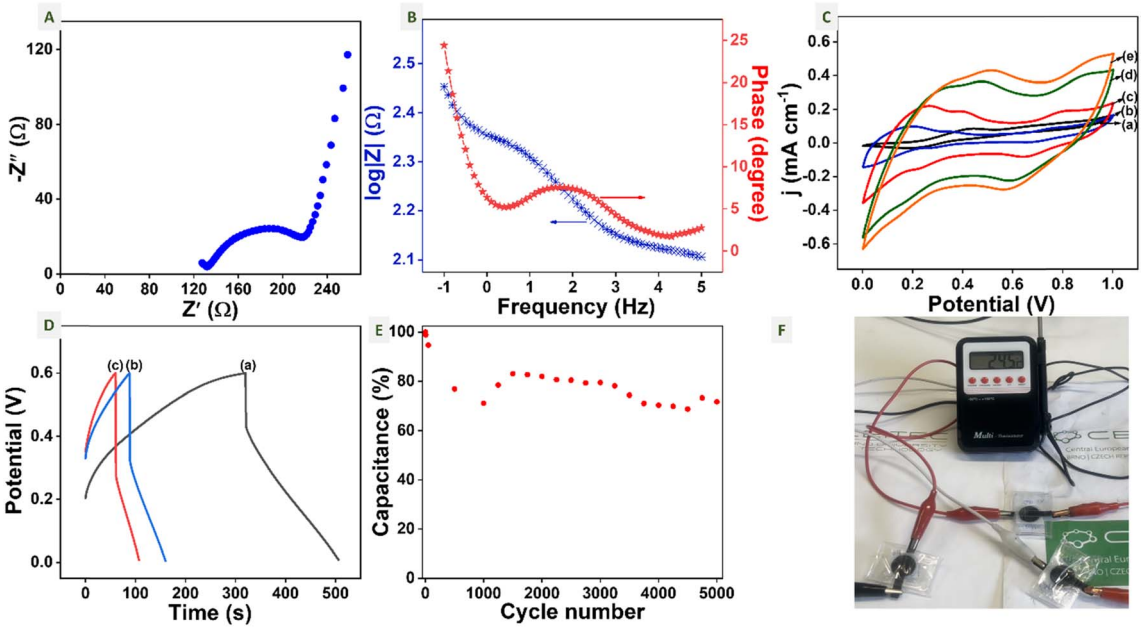

Fig. 6 Electrochemical performance studies of TC-3DE supercapacitors: (A) Nyquist plot, (B) Bode plot, (C) cyclic voltammograms at different scan rates ((a) 1, (b) 5, (c) 25, (d) 75, and (e) 100 mV s^{-1}), (D) GCD curves of the symmetric TC-3DE cell at different current densities ((a) 150, (b) 200 and (c) 250 mA g^{-1}), (E) cycling stability of the symmetric TC-3DE cell and (F) photograph of a timer being powered using TC-3DE cells.

Fig. 6F (see also Video S1†). The cycling stability of the TC-3DE supercapacitor was studied by performing 5000 cycles of CV (shown in Fig. S6(B)†). The supercapacitor retained 73% of its initial capacitance at the 5000th cycle, as shown in Fig. 6E.

Recycling of used 3D-printed supercapacitors and applications

The used 3D printed supercapacitors were recycled to obtain conductive carbon black in the 3D printed electrodes. The cells were disassembled to collect the electrodes. The collected electrodes were sonicated in de-ionised water for an hour and in ethanol for 30 min. Then, the cleaned electrodes were added into an aqueous solution of 1 M NaOH and left for 12 hours. Then the solution was sonicated for 30 min to dissolve the 3D printed electrodes. The obtained black colored solution was centrifuged to obtain the carbon black (CB). The supernatant solution is the sodium salt of lactic acid and the precipitate is the conductive carbon black. The supernatant was later filtered to utilize as electrolyte and the precipitate was washed multiple times with DIW and ethanol to utilize as the conductive additive in the electrodes. The washed CB was dried in a vacuum oven at 60 °C overnight and named RCB.

For comparison, carbon black is extracted from a fresh PLA/conductive graphene filament using the same procedure and named 3DE-CB.

The supernatant is the sodium salt of lactic acid (sodium lactate), which can be utilized as an electrolyte for supercapacitors. The cyclic voltammogram of 1 M sodium salt of lactic acid as electrolyte in comparison with 1 M H_2SO_4 to study a sodium composite material working electrode is shown in Fig. S7(A).† From CV, we can clearly see that the recycled sodium lactate can be utilized as an electrolyte. The area under the curves for 1 M H_2SO_4 and 1 M sodium lactate is 0.86 mA V and 0.77 mA V, respectively, which suggests that the recycled sodium salt of lactic acid can be reused as an electrolyte in supercapacitors.

Further, the SEM image and XRD pattern of the recycled carbon black (RCB) are shown in Fig. 7A and B respectively. We can observe that the conductive component is conductive carbon nanotubes, which is also confirmed from the XRD pattern of the RCB. The XRD pattern confirms the absence of PLA and other impurities in RCB. Both the XRD pattern and the SEM image of RCB are identical to the XRD pattern and SEM image of 3DE-CB shown in Fig. S8(A) and (B),† which indicates the absence of MXene and other impurities from the used supercapacitor.

The RCB was used as the conductive additive in the cathode of sodium-ion batteries with MSTC-OX as the active material, which is named SIB-a. For comparison, a cell with super-p carbon black (SPCB) was also constructed with MSTC-OX as the active material and is named SIB-b. Fig. 7C shows the Nyquist plots of SIB-a and SIB-b cells. Both plots fit with an equivalent circuit $R_s + (C_{dl}/R_{ct}) + W$ with a semicircle in the higher frequency region and a tail in the lower frequency region. The total and charge transfer impedances of SIB-a and SIB-b are similar. The total resistance or solution resistance (R_s) of both cells is ~10 Ω. The charge transfer resistance (R_{ct}) of SIB-a is 526 Ω and that of SIB-b is 516 Ω, respectively. The double layer capacitance (C_{dl}) of SIB-a and SIB-b cells is 2.1 μF and 2.7 μF, respectively.

To study the performance of SIB-a, galvanostatic charge–discharge is performed at different current rates and compared with that of SIB-b. The initial discharge capacity of SIB-a and

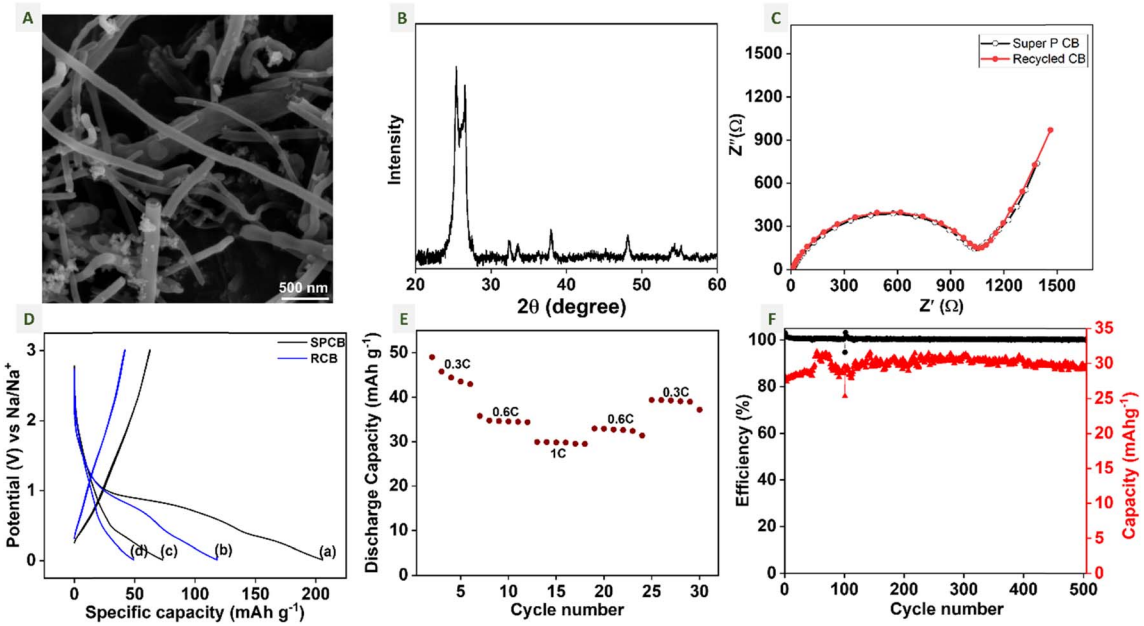

Fig. 7 Studies of recycled carbon black: (A) SEM and (B) XRD images of recycled carbon black. (C) Nyquist plots and (D) GCD (at 0.3C rate) of SIB-a ((a)-cycle 1 and (c)-cycle 2) and SIB-b ((b)-cycle 1 and (d)-cycle 2) cells. (E) Rate capability and (F) coulombic efficiency and discharge capacity (1C rate) of SIB-a.

SIB-b is 120 mA h g^{-1} and 207 mA h g^{-1} at a current of 0.3C, respectively, as shown in Fig. 7D. In both cases, the capacity was reduced to ~40% during the second cycle and stabilized in further cycles. To learn more about SIB-a, rate capability was studied at 0.3C, 0.6C and 1C current rates (Fig. 7E). The cell retained 40 mA h g^{-1} capacity at a 0.66C rate even after high current density cycles. The cycling stability of SIB-a and SIB-b is studied using GCD at a 1C rate, as shown in Fig. S9.† Also, the cell has 100% coulombic efficiency and a high capacity retention after 500 cycles at a 1C current rate, as shown in Fig. 7F. The performance of RCB is comparable with that of the 3DE-CB cell (SIB-c) at a 0.3C rate, which has an initial capacity of ~110 mA h g^{-1} and reduced to ~40mA h g^{-1} in further cycles (Fig. S8(D)†). This shows that the recycled carbon black from the used supercapacitors can be as good as the carbon black extracted from the fresh 3D filament. This shows the promise of recyclable materials for the purpose of energy storage.

As a demonstration of practical application, a glucometer was powered using SIB-a cells and measured the concentration of D-glucose solution as shown in Fig. S7B† (also see ESI Video S2†). Overall, the recycled carbon black can be an alternative to Super-P carbon black in electrode materials for energy storage applications. Also, PLA based 3D printed electrodes can be recycled to extract lactic acid and additives which can then be utilized in different applications without contributing to e-waste.

Conclusion

Usually, MXenes are synthesised from their MAX phases using harsh chemicals like hydrogen fluoride (HF). Recently, the HF-free molten salt method has been developed to etch MAX phases at higher temperature as an alternative. However, high temperatures affect the properties of MXenes. To avoid the high temperature during synthesis, we have proposed oxalic acid as an organic additive to lower the etching temperature of Ti_3AlC_2 to 400 °C in molten salt synthesis, which can also be scalable to the industrial level. Further, recyclable and environmentally safe $Ti_3C_2T_x$ based 3D printed supercapacitors are designed using modified conductive graphene/polylactic acid (PLA) 3D printed electrodes and xanthan-gum gel electrolyte. The symmetric 3D-printed supercapacitors have a high specific capacitance of 30 F g^{-1} at a current density of 150 mA g^{-1} with an energy density and a power density of 1.767 W h kg^{-1} and 20.64 W kg^{-1}, respectively. Further, to prevent the landfilling of used supercapacitors as e-waste, 3D-printed electrodes are recovered and recycled. Recycled conductive carbon is utilized as a conductive additive in the anode material of sodium-ion batteries (SIBs) to power a glucometer. The sodium salt of lactic acid (sodium lactate) obtained during the recycling process is demonstrated as an electrolyte for supercapacitors. This work established an eco-friendly synthesis method to etch MAX phases and also the use of recyclable 3D printed electrodes in energy storage applications to ensure the complete utilization of resources for environmental safety.

Data availability

Data for this article are available at ZENODO at **https://zenodo.org**.

Conflicts of interest

There is no conflict of interest.

Author contributions

M. P. and B. K. conceptualized the idea. B. K. planned and executed the experiments and wrote the manuscript. M. P. set directions, supervised the work and reviewed the manuscript. The manuscript was written through contributions of all authors. All authors have given approval to the final version of the manuscript.

Acknowledgements

The work was supported by the ERDF/ESF project TECHSCALE (No. CZ.02.01.01/00/22_008/0004587). This research was co-funded by the European Union under the REFRESH-Research Excellence For REgion Sustainability and High-tech Industries project number CZ.10.03.01/00/22_003/0000048 *via* the Operational Programme Just Transition. B. K. would like to thank the Ministry of Education, Youth and Sports for the financial support for the project IMPROV V/CZ.02.01.01/00/22_010/0002552. B. K. would like to thank the CEITEC Nano Research Infrastructure supported by MEYS CR (LM2018110) for providing spectroscopic and microscopic characterization facilities. B. K. acknowledges the help of Mr S. Mappoli and Dr K. Manoharan with the videos. The authors would like to thank Dr Senthilnathan Natarajan for proofreading the manuscript.

References

1 S. Natarajan, M. L. Divya and V. Aravindan, Should we recycle the graphite from spent lithium-ion batteries? The untold story of graphite with the importance of recycling, *J. Energy Chem.*, 2022, **71**, 351–369, DOI: **10.1016/j.jechem.2022.04.012**.

2 M. Jacoby, It's time to get serious about recycling lithium-ion batteries, *Chem. Eng. News*, 2019, **97**(28), 29–32.

3 G. Harper, R. Sommerville, E. Kendrick, L. Driscoll, P. Slater, R. Stolkin, A. Walton, P. Christensen, O. Heidrich, S. Lambert, *et al.*, Recycling lithium-ion batteries from electric vehicles, *Nature*, 2019, **575**(7781), 75–86, DOI: **10.1038/s41586-019-1682-5**.

4 Y. Li, S. Wang, S. Qian, Z. Liu, Y. Weng and Y. Zhang, Depolymerization and Re/Upcycling of Biodegradable PLA Plastics, *ACS Omega*, 2024, **9**(12), 13509–13521, DOI: **10.1021/acsomega.3c08674**.

5 Y. Nishioka, K. Nagano, Y. Koga, Y. Okada, I. Mori, A. Hayase, T. Mori and K. Manabe, Lactic acid as a major contributor to hand surface infection barrier and its association with morbidity to infectious disease, *Sci. Rep.*, 2021, **11**(1), 18608, DOI: **10.1038/s41598-021-98042-4**.

6 M. P. Browne and M. Pumera, Impurities in graphene/PLA 3D-printing filaments dramatically influence the electrochemical properties of the devices, *Chem. Commun.*, 2019, **55**(58), 8374–8377, DOI: **10.1039/C9CC03774H**.

7 W. Nie, L. Liu, Q. Li, S. Zhang, J. Hu, X. Yang and X. Ding, A wearable fiber-shaped supercapacitor based on a poly(lactic acid) filament and high loading polypyrrole, *RSC Adv.*, 2019, **9**(33), 19180–19188, DOI: **10.1039/C9RA02171J**.

8 K. Ghosh, S. Ng, C. Iffelsberger and M. Pumera, Inherent Impurities in Graphene/Polylactic Acid Filament Strongly Influence on the Capacitive Performance of 3D-Printed Electrode, *Chem.–Eur. J.*, 2020, **26**(67), 15746–15753, DOI: **10.1002/chem.202004250**.

9 D. C. Carvalho Fernandes, D. Lynch and V. Berry, 3D-printed graphene/polymer structures for electron-tunneling based devices, *Sci. Rep.*, 2020, **10**(1), 11373, DOI: **10.1038/s41598-020-68288-5**.

10 S. Subhadarshini, K. Ghosh and M. Pumera, Multiscale hierarchical nanoarchitectonics with stereographically 3D-printed electrodes for water splitting and energy storage, *Mater. Today*, 2024, **74**, 34–45, DOI: **10.1016/j.mattod.2024.02.004**.

11 K. Ghosh and M. Pumera, Free-standing electrochemically coated MoSx based 3D-printed nanocarbon electrode for solid-state supercapacitor application, *Nanoscale*, 2021, **13**(11), 5744–5756, DOI: **10.1039/D0NR06479C**.

12 G. Zhu, Y. Hou, J. Lu, H. Zhang, Z. Zhuang, M. M. Baig, M. Z. Khan, M. A. Akram, S. Dong, P. Liu, *et al.*, MXene decorated 3D-printed carbon black-based electrodes for solid-state micro-supercapacitors, *J. Mater. Chem. A*, 2023, **11**(46), 25422–25428, DOI: **10.1039/D3TA04573K**.

13 A. Bhat, S. Anwer, K. S. Bhat, M. I. H. Mohideen, K. Liao and A. Qurashi, Prospects challenges and stability of 2D MXenes for clean energy conversion and storage applications, *npj 2D Mater. Appl.*, 2021, **5**(1), 61, DOI: **10.1038/s41699-021-00239-8**.

14 Y. Wei, P. Zhang, R. A. Soomro, Q. Zhu and B. Xu, Advances in the Synthesis of 2D MXenes, *Adv. Mater.*, 2021, **33**(39), 2103148, DOI: **10.1002/adma.202103148**.

15 C. E. Shuck, M. Han, K. Maleski, K. Hantanasirisakul, S. J. Kim, J. Choi, W. E. B. Reil and Y. Gogotsi, Effect of Ti3AlC2 MAX Phase on Structure and Properties of Resultant Ti3C2Tx MXene, *ACS Appl. Nano Mater.*, 2019, **2**(6), 3368–3376, DOI: **10.1021/acsanm.9b00286**.

16 A. Zhou, Y. Liu, S. Li, X. Wang, G. Ying, Q. Xia and P. Zhang, From structural ceramics to 2D materials with multi-applications: a review on the development from MAX phases to MXenes, *J. Adv. Ceram.*, 2021, **10**(6), 1194–1242, DOI: **10.1007/s40145-021-0535-5**.

17 C. Rong, T. Su, Z. Li, T. Chu, M. Zhu, Y. Yan, B. Zhang and F.-Z. Xuan, Elastic properties and tensile strength of 2D Ti3C2Tx MXene monolayers, *Nat. Commun.*, 2024, **15**(1), 1566, DOI: **10.1038/s41467-024-45657-6**.

18 H. Zhang, Ultrathin Two-Dimensional Nanomaterials, *ACS Nano*, 2015, **9**(10), 9451–9469, DOI: **10.1021/acsnano.5b05040**.

19 M. Naguib, V. N. Mochalin, M. W. Barsoum and Y. Gogotsi, 25th Anniversary Article: MXenes: A New Family of Two-Dimensional Materials, *Adv. Mater.*, 2014, **26**(7), 992–1005, DOI: **10.1002/adma.201304138**.

20 M. Naguib, O. Mashtalir, J. Carle, V. Presser, J. Lu, L. Hultman, Y. Gogotsi and M. W. Barsoum, Two-Dimensional Transition Metal Carbides, *ACS Nano*, 2012, **6**(2), 1322–1331, DOI: **10.1021/nn204153h**.

21 M. Naguib, J. Halim, J. Lu, K. M. Cook, L. Hultman, Y. Gogotsi and M. W. Barsoum, New Two-Dimensional Niobium and Vanadium Carbides as Promising Materials for Li-Ion Batteries, *J. Am. Chem. Soc.*, 2013, **135**(43), 15966–15969, DOI: **10.1021/ja405735d**.

22 K. A. Novčić, C. Iffelsberger, M. Palacios-Corella and M. Pumera, Solvents dramatically influence the atomic composition and catalytic properties of Ti3C2Tx MXenes, *J. Mater. Chem. A*, 2023, **11**(25), 13419–13431, DOI: **10.1039/D3TA01441J**, DOI: **10.1039/D3TA01441J**.

23 M. Urso, M. Ussia, F. Novotný and M. Pumera, Trapping and detecting nanoplastics by MXene-derived oxide microrobots, *Nat. Commun.*, 2022, **13**(1), 3573, DOI: **10.1038/s41467-022-31161-2**.

24 M. Okubo, A. Sugahara, S. Kajiyama and A. Yamada, MXene as a Charge Storage Host, *Acc. Chem. Res.*, 2018, **51**(3), 591–599, DOI: **10.1021/acs.accounts.7b00481**.

25 S. Kumar, M. A. Rehman, S. Lee, M. Kim, H. Hong, J.-Y. Park and Y. Seo, Supercapacitors based on Ti3C2Tx MXene extracted from supernatant and current collectors passivated by CVD-graphene, *Sci. Rep.*, 2021, **11**(1), 649, DOI: **10.1038/s41598-020-80799-9**.

26 M. B. Riaz, D. Hussain, S. U. Awan, S. Rizwan, S. Zainab and S. A. Shah, 2-Dimensional Ti3C2Tx/NaF nano-composites as electrode materials for hybrid battery-supercapacitor applications, *Sci. Rep.*, 2024, **14**(1), 1654, DOI: **10.1038/s41598-024-52280-4**.

27 M. Depijan, K. Hantanasirisakul and P. Pakawatpanurut, Interfacial Engineering of Ti3C2Tx MXene Electrode Using g-C3N4 Nanosheets for High-Performance Supercapacitor in Neutral Electrolyte, *ACS Omega*, 2024, **9**(20), 22256–22264, DOI: **10.1021/acsomega.4c01353**.

28 A. Gentile, S. Marchionna, M. Balordi, G. Pagot, C. Ferrara, V. Di Noto and R. Ruffo, Critical Analysis of MXene Production with In-Situ HF Forming Agents for Sustainable Manufacturing, *ChemElectroChem*, 2022, **9**(23), e202200891, DOI: **10.1002/celc.202200891**.

29 L. Zhang, W. Song, H. Liu, H. Ding, Y. Yan and R. Chen, Influencing Factors on Synthesis and Properties of MXene: A Review, *Processes*, 2022, **10**(9), 1744.

30 U. Khan, Y. Luo, L. B. Kong and W. Que, Synthesis of fluorine free MXene through lewis acidic etching for application as electrode of proton supercapacitors, *J. Alloys Compd.*, 2022, **926**, 166903, DOI: **10.1016/j.jallcom.2022.166903**.

31 C. Peng, P. Wei, X. Chen, Y. Zhang, F. Zhu, Y. Cao, H. Wang, H. Yu and F. Peng, A hydrothermal etching route to synthesis of 2D MXene (Ti3C2, Nb2C): enhanced exfoliation and improved adsorption performance, *Ceram. Int.*, 2018, **44**(15), 18886–18893, DOI: **10.1016/j.ceramint.2018.07.124**.

32 C. Wang, H. Shou, S. Chen, S. Wei, Y. Lin, P. Zhang, Z. Liu, K. Zhu, X. Guo, X. Wu, *et al.*, Mxene Synthesis: HCl-Based Hydrothermal Etching Strategy toward Fluoride-Free MXenes (Adv. Mater. 27/2021), *Adv. Mater.*, 2021, **33**(27), 2170209, DOI: **10.1002/adma.202170209**.

33 Y. Guo, X. Zhang, S. Jin, Q. Xia, Y. Chang, L. Wang and A. Zhou, Synthesis of Mo2C MXene with high electrochemical performance by alkali hydrothermal etching, *J. Adv. Ceram.*, 2023, **12**(10), 1889–1901, DOI: **10.26599/JAC.2023.9220795**.

34 C. Wang, H. Shou, S. Chen, S. Wei, Y. Lin, P. Zhang, Z. Liu, K. Zhu, X. Guo, X. Wu, *et al.*, HCl-Based Hydrothermal Etching Strategy toward Fluoride-Free MXenes, *Adv. Mater.*, 2021, **33**(27), 2101015, DOI: **10.1002/adma.202101015**.

35 P. Urbankowski, B. Anasori, T. Makaryan, D. Er, S. Kota, P. L. Walsh, M. Zhao, V. B. Shenoy, M. W. Barsoum and Y. Gogotsi, Synthesis of two-dimensional titanium nitride Ti4N3 (MXene), *Nanoscale*, 2016, **8**(22), 11385–11391, DOI: **10.1039/C6NR02253G**, DOI: **10.1039/C6NR02253G**.

36 J. Chen, Q. Jin, Y. Li, H. Shao, P. Liu, Y. Liu, P.-L. Taberna, Q. Huang, Z. Lin and P. Simon, Molten Salt-Shielded Synthesis (MS3) of MXenes in Air, *Energy Environ. Mater.*, 2023, **6**(2), e12328, DOI: **10.1002/eem2.12328**.

37 G. Ma, H. Shao, J. Xu, Y. Liu, Q. Huang, P.-L. Taberna, P. Simon and Z. Lin, Li-ion storage properties of two-dimensional titanium-carbide synthesized via fast one-pot method in air atmosphere, *Nat. Commun.*, 2021, **12**(1), 5085, DOI: **10.1038/s41467-021-25306-y**.

38 J. Muñoz, M. Palacios-Corella and M. Pumera, Electrically reading a light-driven molecular switch on 2D-Ti3C2Tx MXene via molecular engineering: towards responsive MXetronics, *J. Mater. Chem. A*, 2022, **10**(32), 17001–17008, DOI: **10.1039/D2TA03349F**, DOI: **10.1039/D2TA03349F**.

39 K. Arole, J. W. Blivin, S. Saha, D. E. Holta, X. Zhao, A. Sarmah, H. Cao, M. Radovic, J. L. Lutkenhaus and M. J. Green, Water-dispersible Ti3C2Tz MXene nanosheets by molten salt etching, *iScience*, 2021, **24**(12), 103403, DOI: **10.1016/j.isci.2021.103403**.

40 Y. Wang, Z. Gao, X. Zhang and M. Shen, Modulation of the Cobalt Content in Ti3C2Tx by Molten Salt Method for Hydrogen Evolution Reaction, *J. Electrochem. So.*, 2024, **171**(1), 016502, DOI: **10.1149/1945-7111/ad1b79**.

41 O. Mashtalir, M. Naguib, B. Dyatkin, Y. Gogotsi and M. W. Barsoum, Kinetics of aluminum extraction from Ti3AlC2 in hydrofluoric acid, *Mater. Chem. Phys.*, 2013, **139**(1), 147–152, DOI: **10.1016/j.matchemphys.2013.01.008**.

42 A. Syuy, D. Shtarev, A. Lembikov, M. Gurin, R. Kevorkyants, G. Tselikov, A. Arsenin and V. Volkov, Effective Method for the Determination of the Unit Cell Parameters of New MXenes, *Materials*, 2022, **15**(24), 8798.

43 J. Zhang, K. A. S. Usman, M. A. N. Judicpa, D. Hegh, P. A. Lynch and J. M. Razal, Applications of X-Ray-Based Characterization in MXene Research, *Small Methods*, 2023, **7**(8), 2201527, DOI: **10.1002/smtd.202201527**.

44 A. Iqbal and N. M. Hamdan, Investigation and Optimization of Mxene Functionalized Mesoporous Titania Films as Efficient Photoelectrodes, *Materials*, 2021, **14**(21), 6292.

45 C. Zhao, Q. Wang, H. Zhang, S. Passerini and X. Qian, Two-Dimensional Titanium Carbide/RGO Composite for High-Performance Supercapacitors, *ACS Appl. Mater. Interfaces*, 2016, **8**(24), 15661–15667, DOI: **10.1021/acsami.6b04767**.

46 M.-L. Kung, P.-Y. Lin, C.-W. Hsieh and S. Hsieh, Aqueous self-assembly and surface-functionalized nanodots for live cell imaging and labeling, *Nano Res.*, 2014, **7**(8), 1164–1176, DOI: **10.1007/s12274-014-0479-y**.

47 L.-Å. Näslund, P. O. Å. Persson and J. Rosen, X-ray Photoelectron Spectroscopy of Ti3AlC2, Ti3C2Tz, and TiC Provides Evidence for the Electrostatic Interaction between Laminated Layers in MAX-Phase Materials, *J. Phys. Chem. C*, 2020, **124**(50), 27732–27742, DOI: 10.1021/acs.jpcc.0c07413.

48 P. Visser, Y. Gonzalez-Garcia, J. M. C. Mol and H. Terryn, Mechanism of Passive Layer Formation on AA2024-T3 from Alkaline Lithium Carbonate Solutions in the Presence of Sodium Chloride, *J. Electrochem. Soc.*, 2018, **165**(2), C60, DOI: 10.1149/2.1011802jes.

49 B. K. Singh, Y. Kim, S. Kwon and K. Na, Selective Catalytic Transfer Hydrogenolysis of Glycerol to 2-Isopropoxy-Propan-1-Ol over Noble Metal Ion-Exchanged Mordenite Zeolite, *Catalysts*, 2019, **9**(11), 885.

50 E. Hoque, J. A. DeRose, G. Kulik, P. Hoffmann, H. J. Mathieu and B. Bhushan, Alkylphosphonate Modified Aluminum Oxide Surfaces, *J. Phys. Chem. B*, 2006, **110**(22), 10855–10861, DOI: 10.1021/jp061327a.

51 V. Natu, M. Benchakar, C. Canaff, A. Habrioux, S. Célérier and M. W. Barsoum, A critical analysis of the X-ray photoelectron spectra of Ti3C2Tz MXenes, *Matter*, 2021, **4**(4), 1224–1251, DOI: 10.1016/j.matt.2021.01.015.

52 Z. Viskadourakis, G. Perrakis, E. Symeou, J. Giapintzakis and G. Kenanakis, Transport properties of 3D printed polymer nanocomposites for potential thermoelectric applications, *Appl. Phys. A*, 2019, **125**(3), 159, DOI: 10.1007/s00339-019-2469-0.

53 S. Sasi, A. Murali, S. V. Nair, A. S. Nair and K. R. V. Subramanian, The effect of graphene on the performance of an electrochemical flow capacitor, *J. Mater. Chem. A*, 2015, **3**(6), 2717–2725, DOI: 10.1039/C4TA05785F.

54 J. Vigneshwaran, J. Jose, S. Thomas, A. Gagliardi, M. Thelakkat and S. P. Jose, Flexible quasi-solid-state supercapacitors based on Ti3C2-Polypyrrole nanocomposites, *Electrochim. Acta*, 2022, **429**, 141051, DOI: 10.1016/j.electacta.2022.141051.

55 J. Yin, K. Wei, J. Zhang, S. Liu, X. Wang, X. Wang, Q. Zhang, Z. Qin and T. Jiao, MXene-based film electrode and all-round hydrogel electrolyte for flexible all-solid supercapacitor with extremely low working temperature, *Cell Rep. Phys. Sci.*, 2022, **3**(5), 100893, DOI: 10.1016/j.xcrp.2022.100893.

56 A. Oz, S. Hershkovitz, N. Belman, E. Tal-Gutelmacher and Y. Tsur, Analysis of impedance spectroscopy of aqueous supercapacitors by evolutionary programming: finding DFRT from complex capacitance, *Solid State Ionics*, 2016, **288**, 311–314, DOI: 10.1016/j.ssi.2015.11.008.

57 X. Pang, X. Liu and B. Jin, Microstructure Changes of Ti-Al-C Films Deposited by Filtered Cathodic Vacuum, *Arc. J. Nanomater.*, 2014, **2014**, 286484, DOI: 10.1155/2014/286484.

58 S. A. Melchior, K. Raju, I. S. Ike, R. M. Erasmus, G. Kabongo, I. Sigalas, S. E. Iyuke and K. I. Ozoemena, High-Voltage Symmetric Supercapacitor Based on 2D Titanium Carbide (MXene, Ti2CTx)/Carbon Nanosphere Composites in a Neutral Aqueous Electrolyte, *J. Electrochem. Soc.*, 2018, **165**(3), A501, DOI: 10.1149/2.0401803jes.

59 C. C. L. McCrory, S. Jung, J. C. Peters and T. F. Jaramillo, Benchmarking Heterogeneous Electrocatalysts for the Oxygen Evolution Reaction, *J. Am. Chem. Soc.*, 2013, **135**(45), 16977–16987, DOI: 10.1021/ja407115p.

60 B. K, K. Sridharan, M. A. K, H. N. Lim and H. S. Nagaraja, Microwave assisted growth of stannous ferrite microcubes as electrodes for potentiometric nonenzymatic H2O2 sensor and supercapacitor applications, *Electrochim. Acta*, 2016, **217**, 139–149, DOI: 10.1016/j.electacta.2016.09.083.

61 V. Ganesh, S. Pitchumani and V. Lakshminarayanan, New symmetric and asymmetric supercapacitors based on high surface area porous nickel and activated carbon, *J. Power Sources*, 2006, **158**(2), 1523–1532, DOI: 10.1016/j.jpowsour.2005.10.090.

62 Y. Zhou, H. Xu, N. Lachman, M. Ghaffari, S. Wu, Y. Liu, A. Ugur, K. K. Gleason, B. L. Wardle and Q. M. Zhang, Advanced asymmetric supercapacitor based on conducting polymer and aligned carbon nanotubes with controlled nanomorphology, *Nano Energy*, 2014, **9**, 176–185, DOI: 10.1016/j.nanoen.2014.07.007.

63 F. Barzegar, A. Bello, D. Y. Momodu, J. K. Dangbegnon, F. Taghizadeh, M. J. Madito, T. M. Masikhwa and N. Manyala, Asymmetric supercapacitor based on an α-MoO3 cathode and porous activated carbon anode materials, *RSC Adv.*, 2015, **5**(47), 37462–37468, DOI: 10.1039/C5RA03579A.

64 M. Kulka and A. Pertek, Microstructure and properties of borocarburized 15CrNi6 steel after laser surface modification, *Appl. Surf. Sci.*, 2004, **236**(1), 98–105, DOI: 10.1016/j.apsusc.2004.04.005.

65 G. Zhao, N. Zhang and K. Sun, Porous MoO3 films with ultra-short relaxation time used for supercapacitors, *Mater. Res. Bull.*, 2013, **48**(3), 1328–1332, DOI: 10.1016/j.materresbull.2012.11.080.